

# Nanoscale Control of Domain Architectures in BiFeO<sub>3</sub> Thin Films

Ying-Hao Chu,<sup>\*,†</sup> Qing He,<sup>‡</sup> Chan-Ho Yang,<sup>‡</sup> Pu Yu,<sup>‡</sup> Lane W. Martin,<sup>§</sup>  
Padraic Shafer,<sup>||</sup> and R. Ramesh<sup>‡,§,||</sup>

*Department of Materials Science and Engineering, National Chiao Tung University, HsinChu, Taiwan 30010, Republic of China, Department of Physics, University of California, Berkeley, California 94720, Materials Science Division, Lawrence Berkeley National Laboratory, Berkeley, California 94720, and Department of Materials Science and Engineering, University of California, Berkeley, California 94720*

Received March 8, 2009

## ABSTRACT

We demonstrate an approach to create a one-dimensional nanoscale array of domain walls in epitaxial La-substituted BiFeO<sub>3</sub> films. We have used a DyScO<sub>3</sub> (110)<sub>o</sub> single-crystal substrate to provide an anisotropic strain to exclude two of the possible structural variants. Furthermore, through careful control of electrostatic boundary conditions, such as the thickness of the SrRuO<sub>3</sub> bottom electrode to induce the self-poling effects, we can choose to obtain either 109° or 71° one-dimensional periodic domain walls. Detailed measurements of the domain structures is shown using piezoresponse force microscopy and X-ray diffraction, which confirms that these periodic structures are the same as those suggested in previous literature.

Recently, the lead-free ferroelectric BiFeO<sub>3</sub> (BFO) has attracted much attention, because of its superior thin-film ferroelectric properties,<sup>1</sup> which are comparable to those of the tetragonal, Ti-rich PZT system. BFO has a high ferroelectric Curie temperature ( $T_c = 850^\circ\text{C}$  in single crystals),<sup>2,3</sup> which enables it to be used reliably at high temperatures. The generic domain structure of rhombohedrally distorted perovskite ferroelectrics has been described in detail by Streiffer et al.<sup>4</sup> This paper showed that 71° domain walls form on the {101} planes; in contrast, 109° domain walls have been predicted to form on {100} planes. In addition, theoretical models have predicted the feasibility of controlling the domain architecture in thin films of BFO through suitable control over the heteroepitaxial constraints.<sup>5</sup> An interesting question then arises: how does one create quasi-periodic nanoscale arrays of ferroelastic domain walls such as the 71° and 109° domain walls in BFO thin films? In this paper, we describe an approach to achieve such structures.

BFO is a room-temperature, single-phase magnetoelectric multiferroic.<sup>1</sup> Recent studies of BFO thin films have shown the existence of a large ferroelectric polarization, as well as a weak ferromagnetic response, which results from a small

canting of the antiferromagnetic moments, because of a Dzyaloshinskii–Moriya interaction of the antiferromagnetic sublattice.<sup>6</sup> BFO is a rhombohedrally distorted perovskite material, which means that the ferroelectric polarization can have orientations along the four pseudo-cubic diagonals ( $\langle 111 \rangle$ ).<sup>7</sup> Domain walls in BFO thin films have been shown to possess interesting properties, such as conducting behavior<sup>8</sup> and magnetic interaction;<sup>9,10</sup> therefore, the ability to control and engineer ordered structures of these domain walls could be important for the potential use of such novel properties at domain walls in the next generation of nanoscale devices.

On the (001)<sub>c</sub> perovskite surface, there are eight possible ferroelectric polarization directions, corresponding to four structural variants of the rhombohedral ferroelectric thin film.<sup>4</sup> (For simplicity, the subscripts “C” and “O” refer to the pseudo-cubic structures for BFO and orthorhombic structures of SrRuO<sub>3</sub> (SRO) and DyScO<sub>3</sub> (DSO), respectively.) Domain patterns can develop with either {100}<sub>c</sub> or {101}<sub>c</sub> boundaries, which correspond to 109° and 71° domain walls, respectively, for (001)<sub>c</sub>-oriented rhombohedral films. Figures 1a and 1b show schematics for the two types of predicted periodic domain walls. In both cases, the individual domains in the patterns are energetically degenerate, and, thus, equal-width stripe patterns are theoretically predicted.

To control the domain architecture, we first tuned the ferroelectric transition temperature ( $T_c$ ) by isovalent substitu-

\* Author to whom correspondence should be addressed. E-mail: yhc@cc.nctu.edu.tw.

<sup>†</sup> Department of Materials Science and Engineering, National Chiao Tung University.

<sup>‡</sup> Department of Physics, University of California.

<sup>§</sup> Materials Science Division, Lawrence Berkeley National Laboratory.

<sup>||</sup> Department of Materials Science and Engineering, University of California.

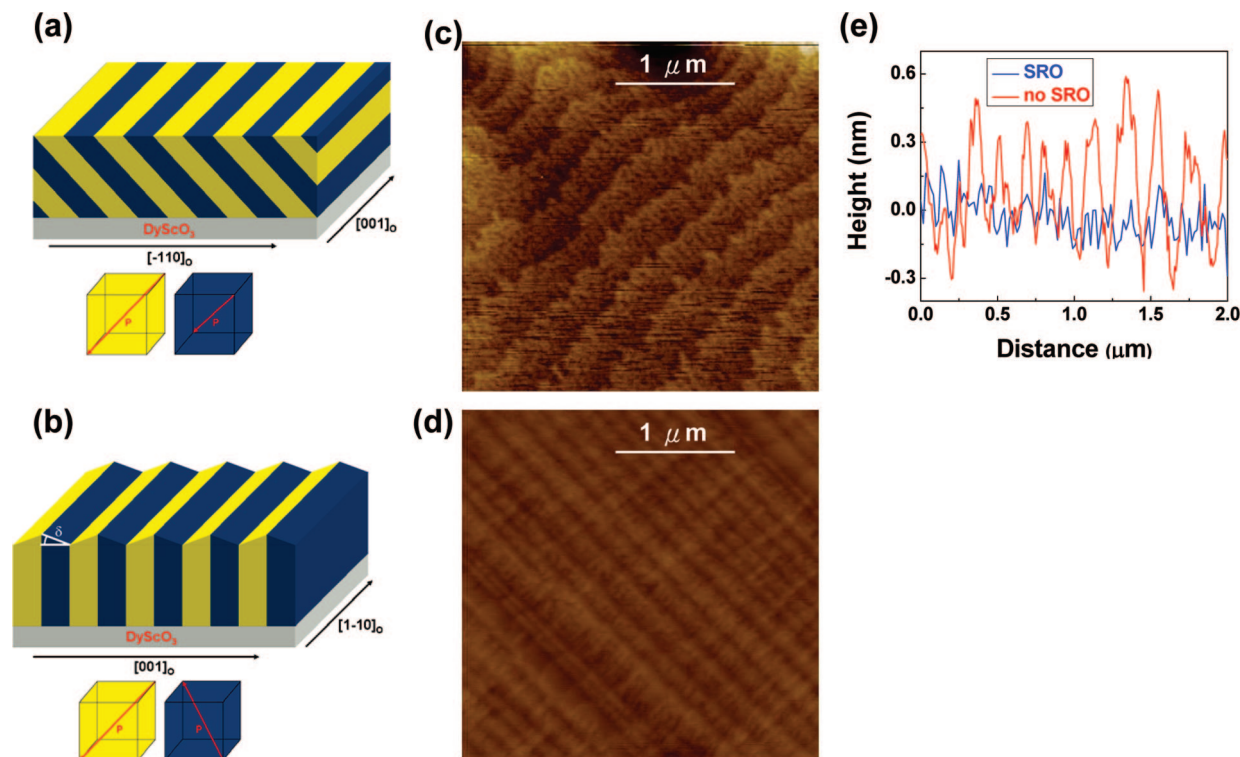


**Figure 1.** Schematics of different domain walls: (a) predicted periodic  $71^\circ$  domain patterns on  $\text{DyScO}_3$  substrates and (b) predicted periodic  $109^\circ$  domain patterns on  $\text{DyScO}_3$  substrates. Also shown is the surface topography, as measured by atomic force microscopy (AFM), for (c) LBFO films grown on a SRO layer and (d) LBFO films grown without a SRO layer. (e) Section analyses on the La-substituted  $\text{BiFeO}_3$  (LBFO) films with and without the SRO layer, showing the “puckering” of the surface for the case of the  $109^\circ$  domain wall arrays.

tion at the Bi site with La (typically 10% La), which has the effect of lowering the  $T_c$  value to  $\sim 600\text{--}650^\circ\text{C}$  (which is below the growth temperature). This concomitantly reduces the lattice parameter of BFO, such that the lattice mismatch to DSO is further reduced.<sup>11</sup> Upon cooling, the phase transformation from the high-temperature cubic phase to the low-temperature rhombohedral phase is assisted by the structural anisotropy in DSO, leading to the selection of two of the four possible structural variants.<sup>12</sup> Previous work has shown that the substrate vicinality<sup>13</sup> can significantly influence the domain evolution; in this work, we have tried to minimize the role of vicinality using substrates with a miscut angle of  $<0.3^\circ$ . Finally, the selection of  $71^\circ$  or  $109^\circ$  domain patterns is dependent on the electrostatic boundary conditions, i.e., the existence of a SRO conducting layer (and its thickness). Qualitatively, in the absence of the conducting SRO layer, the electrostatic boundary conditions at the substrate/film interface favor the formation of  $109^\circ$  domain patterns; when a thick ( $\sim 50$  nm) SRO layer is introduced, the electrostatic boundary condition favors the formation of  $71^\circ$  domain patterns.

LBFO layers (100-nm thick) were deposited on SRO electrodes via pulsed laser deposition at  $700^\circ\text{C}$  and an  $\text{O}_2$  pressure of 100 mTorr, with thicknesses varying from 0 nm to 50 nm. Figure 1c shows the topography of such LBFO films grown on a SRO layer. Because of the coherent growth, the film surface shows large terraces ( $\sim 200$  nm wide) that are atomically flat and separated by small steps varying between one-half and one unit cell in height. However, the LBFO films without a SRO layer show a “puckered”

surface,<sup>4</sup> as shown in Figure 1d. Figure 1e is the section analysis of Figures 1c and 1d, which clearly shows a regular change in height for the LBFO films without a SRO layer. The “puckering” angle can be estimated from such an analysis to be  $\sim 0.34^\circ$ , which also corresponds to structural distortion angle, as determined via X-ray diffraction (XRD) analyses. As a consequence, we expect the LBFO films with a sufficiently thick SRO conducting layer should correspond to the  $71^\circ$  domain structure and the LBFO film without a very thin SRO layer (0–5 nm) should correspond to the  $109^\circ$  domain structure, as shown in Figures 1a and 1b, respectively.

The ferroelectric domain patterns of the areas shown in Figures 1c and 1d were characterized using atomic force microscopy (AFM) (Digital Instruments, Nanoscope-IV Multimode AFM).<sup>14</sup> Piezoresponse force microscopy (PFM) images confirm the dramatic differences in domain structure shown for  $71^\circ$  and  $109^\circ$  domain walls in LBFO. For the  $71^\circ$  domain wall LBFO samples, out-of-plane (OOP) PFM images show uniform contrast (Figure 2a), suggesting that all polarization variants are pointing downward, toward the thick SRO layer. In-plane (IP) PFM images (Figure 2b), taken with the cantilever along  $\langle 110 \rangle_c$ , show a striplike image contrast essentially throughout the entire film. In contrast, for the samples corresponding to Figure 1d, both OOP (Figure 2c) and IP (Figure 2d) PFM images, taken with the cantilever along  $\langle 110 \rangle_c$ , show striplike contrast over large areas; the key difference is the alternating bright and dark contrast in the OOP image (Figure 2c). The change in the OOP contrast signifies a corresponding change in the

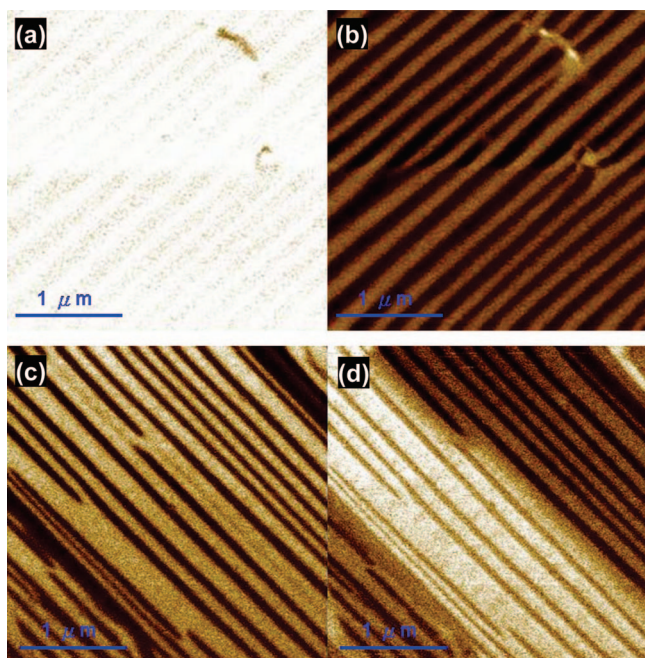


**Figure 2.** Piezoresponse force microscopy (PFM) of different domain patterns, showing (a) out-of-plane (OOP) and (b) in-plane (IP) PFM images of LBFO films with 71° domain in the area of Figure 1c, and (c) OOP and (d) IP PFM images of LBFO films with 109° domain in the area of Figure 1d.

OOP component of the polarization vector, which is consistent with the interpretation of a 109° rotation of the *P*-vector across the wall. We also note that the observed domain walls in Figures 2c and 2d correspond to both the peaks and troughs of the washboard-like schematic in Figure 1b and the surface topography observed in Figure 1d. This result is consistent with the stable configuration predicted for a (001)<sub>C</sub>-oriented rhombohedral ferroelectric film.<sup>4</sup>

Structural characterization was studied via XRD. Reciprocal space mapping (RSM) was performed using a Panalytical X'Pert PRO high-resolution XRD system. The  $\theta$ -2 $\theta$  scans for the LBFO films with 71° and 109° domain walls are shown in Figures 3a and 3b, respectively. No second phase has been detected, which suggests pure-phase LBFO films. Moreover, only the  $\theta$ -2 $\theta$  scan for the LBFO films with 71° domain walls shows the presence of a Keissig fringe pattern, indicating a smoother surface, which is consistent with the AFM data. The full width at half-maximum (fwhm) values of the XRD rocking curves about the 002<sub>C</sub> diffraction peak was measured to be 0.005° for films with 71° domain walls scanned along both the DSO[001]<sub>O</sub> and [110]<sub>O</sub> IP directions (see Figure 3c). In contrast, the corresponding values for films with 109° domain walls scanned along the DSO[110]<sub>O</sub> directions was measured to be 0.01° (see Figure 3d). On the other hand, the rocking curves for this sample measured along the DSO[001]<sub>O</sub> shows two peaks separated by ~0.7° (see Figure 3d). Such a result is consistent with the observed surface topography (shown in Figure 1d). Based on these data, we calculated the monoclinic distortion angle to be ~0.35° along the [001]<sub>O</sub> ([010]<sub>C</sub>) direction, which is, once again, consistent with the AFM data.

To fully understand the structure of these two types of films, XRD RSM was employed.<sup>15</sup> The anisotropic IP compressive strain from the DSO substrate reduces the rhombohedral symmetry (*R3c*) to monoclinic, which has been used as our structural model.<sup>16</sup> In this monoclinic structure (tilted along the  $[\bar{1}\bar{1}0]$ ), the peak positions of the 203 and 023 reciprocal lattice reflections are shifted upward along the *L*-direction and, by contrast, the positions of  $\bar{2}03$  and  $\bar{0}23$  are shifted downward. Based on this model, we measured line scans along the *L*-direction in (*hkl*) RSM for the 203 and 023 reflections. All reciprocal space units are normalized to those of DSO. For the films with 71° domain walls, peak splitting was not observed for the 203 reflection (see Figure 3e), whereas peak splitting was observed for the 023 reflection (see Figure 3f). Similar results were observed for films with 109° domain walls (see the 203 reflection in Figure 3g and the 023 reflection in Figure 3h). These results are consistent with the observation of only two structural variants in both types of films. From these RSM results, we have been able to fully map the structure of the LBFO films. By measuring the splitting between the two peaks, we have calculated the monoclinic distortion to be tilted ~0.51° along the [110] in films with both 71° and 109° domain walls. An additional peak splitting is observed for the LBFO films with 109° domain walls, which is attributed to the “puckered” surface, from which the monoclinic distortion angle can be calculated to be 0.33°, which is, once again, consistent with the AFM and XRD rocking curve data.

The prominent role of the boundary condition (i.e., the bottom electrode) is clearly demonstrated when one studies the effect of the thickness of the SRO layer in the evolution of the domain structure (see Figure 4). Using a combination of both OOP and IP PFM images, we have extracted the relative fraction of 71° and 109° domain walls, as a function of the SRO bottom electrode thickness. Below a SRO thickness of ~5 nm, we observe predominately 109° domain structure. For a SRO thickness in the range of 5–25 nm, there is a mixed domain structure that consists of both 71° and 109° domain walls. On SRO layers that are 25 nm or thicker, BFO films are observed to have predominantly 71° domain walls.

The key question is how the thickness of the SRO layer affects the formation of domain patterns. Two possible scenarios must be verified: strain effects and electrostatic effects. The formation of ferroelastic domains is driven by a need to compensate for the mechanical strain from the rhombohedral distortion of the BFO unit cell. Either 71° or 109° domains have the same structural combination, based on XRD-RSM measurements. Now, if we consider the polarization vectors, with the same structural combination, to partially compensate for the electrostatic field, the stable configuration of 71° domain walls will be in {110}-type planes, and the stable configuration of 109° domain walls will be in {001}-type planes. The 71° and 109° domain samples possess the same structural variants, relative to the DSO substrates, which suggests that the strain state of SRO does not play a significant role in determining the types of the domain patterns. Given that the mismatch for SRO on



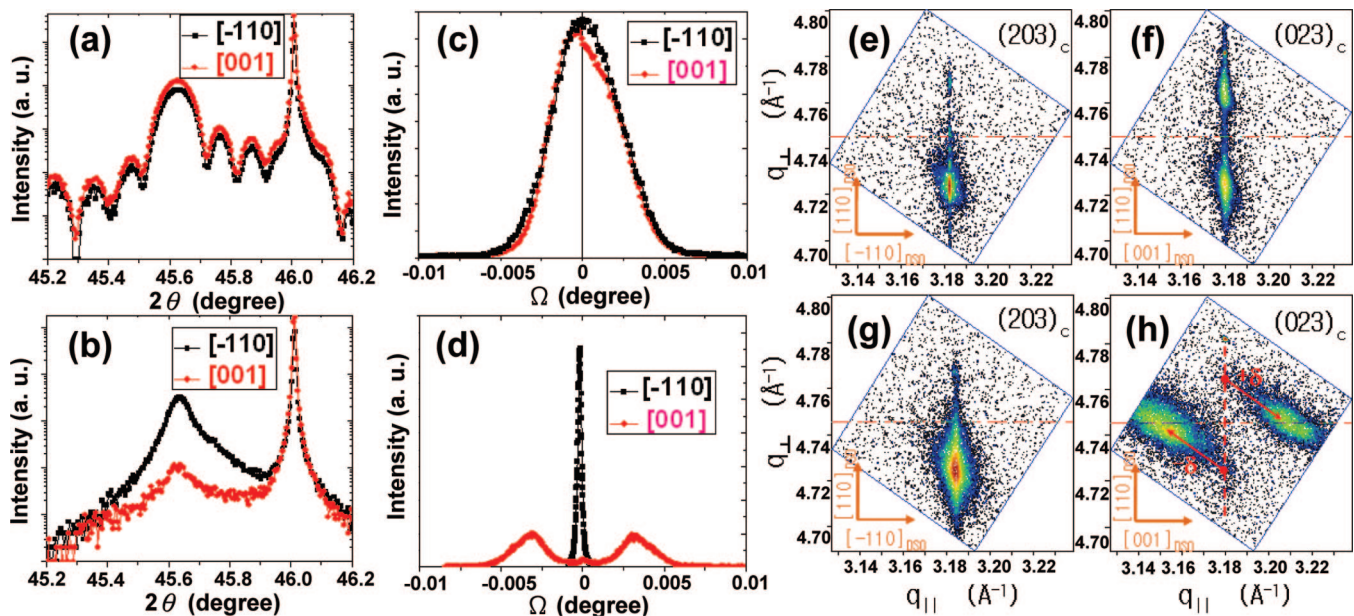


**Figure 3.** Structural characterization, showing XRD  $\theta$ - $2\theta$  scans for a LBFO films (with (a)  $71^\circ$  domain patterns and (b)  $109^\circ$  domain patterns), XRD rocking curves of LBFO films (with (c)  $71^\circ$  domain patterns and (d)  $109^\circ$  domain patterns), and reciprocal space mapping (RSM) scans of LBFO ((e)  $203_c$  RSM scan of LBFO with  $71^\circ$  domain patterns, (f)  $023_c$  RSM scan of LBFO with  $71^\circ$  domain patterns, (g)  $203_c$  RSM scan of LBFO with  $109^\circ$  domain patterns, and (h)  $023_c$  RSM scan of LBFO with  $109^\circ$  domain patterns).

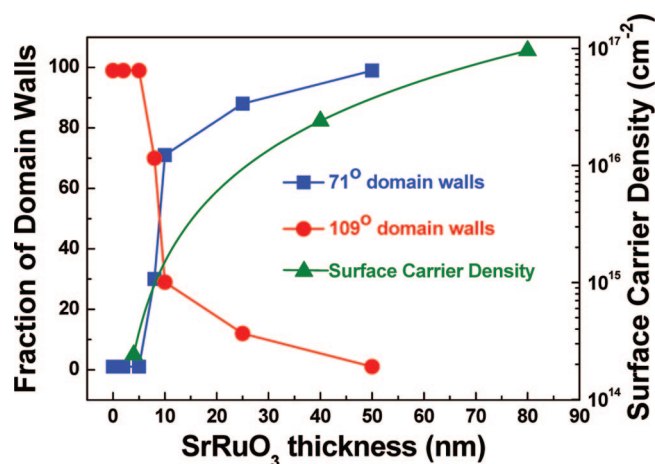


**Figure 4.** Evolution of LBFO domain fractions, as a function of the thickness of the SRO bottom layer.

DSO is relatively small (0.25%), we expect the role of strain relaxation in the SRO layer to be minimal. If one used a conventional Matthews–Blakeslee-type calculation, one obtains a value of  $\sim 20$  nm for the onset of strain relaxation. Moreover, the detailed SRO strain state has been checked using transmission electron microscopy (TEM). Because the crystal structure of SRO is also orthorhombic, we were able to obtain the monodomain SRO on DSO.<sup>12</sup>

The model for this effect is that the spontaneous polarization of the ferroelectric is screened at the electrode/ferroelectric interface by carriers in the electrode.<sup>17</sup> For example, in the case of BFO with a spontaneous polarization of  $\sim 1$  C/m<sup>2</sup> (corresponding to a surface charge of  $\sim 6 \times 10^{14}$  cm<sup>-2</sup>),<sup>18,19</sup> a corresponding surface carrier density would be required in the metal to fully screen the polarization. Within this framework, we can now begin to understand the role of the SRO layer thickness and conductivity in control-

ling the domain structure in the BFO layer. There have been many studies of the thickness dependence of transport properties of epitaxial SRO thin films.<sup>20,21</sup> A common conclusion from these studies is that there is a change in the metallicity as the thickness is reduced. For example, Herranz et al. found an order-of-magnitude change in the room-temperature resistivity ( $\sim 3$  m $\Omega$  cm at a thickness of 4 nm,  $\sim 0.3$  m $\Omega$  cm at a thickness of 40 nm,  $\sim 0.15$  m $\Omega$  cm at a thickness of 80 nm, and no further change is observed in thicker films). With the assumption that the bulk carrier concentration ( $n_0 \approx 1.2 \times 10^{22}$  cm<sup>-3</sup> at 200 K)<sup>22</sup> corresponds to the resistivity of 0.15 m $\Omega$  cm, we have estimated the number of carriers for a 40-nm-thick and 4-nm-thick SRO film to be  $\sim 2.4 \times 10^{16}$  cm<sup>-2</sup> and  $\sim 2.4 \times 10^{14}$  cm<sup>-2</sup>, respectively, as plotted in Figure 4. Thus, we expect complete screening at the ferroelectric/electrode interface for SRO films that are  $\sim 10$  nm thick, which is consistent with our experimental data (see Figure 4).

In summary, we have demonstrated an elegant approach to control the domain variants in LBFO thin films to obtain one-dimensional, quasi-periodic nanoscale arrays of domain walls. Implementation of this approach is demonstrated on DSO substrates where the constraints that are imposed by heteroepitaxy, as well as the use of a SRO layer to break the elastic and electrostatic boundary conditions, can be manipulated to create long-range arrays of domain walls (either  $71^\circ$  or  $109^\circ$  domain walls) in LBFO. This result provides us with set of model systems to further explore the multifunctional properties on the nanoscale domain walls, which may be used as a functional component in novel applications.

**Acknowledgment.** The work at Berkeley is supported by the Director, Office of Science, Office of Basic Energy

Sciences, Materials Sciences Division of the U.S. Department of Energy (under Contract No. DE-AC02-05CH1123). Y.H.C. would also like to acknowledge the support of the National Science Council, R.O.C. (under Contract No. NSC 97-3114-M-009-001). C.H.Y. would like to acknowledge the Korea Research Foundation Grant funded by the Korean Government (MOEHRD) (No. KRF-2006-214-C00020).

## References

- (1) Ramesh, R.; Spaldin, N. A. *Nat. Mater.* **2007**, *6*, 21–29.
- (2) Venevtsev, Yu. N.; Zhadanov, G.; Solov'ev, S. *Sov. Phys. Crystallogr.* **1960**, *4*, 538.
- (3) Smolenskii, G.; Isupov, V.; Agrannovskaya, A.; Kranik, N. *Sov. Phys. Solid State* **1961**, *2*, 2651.
- (4) Streiffer, S. K.; Parker, C. B.; Romanov, A. E.; Lefevre, M. J.; Zhao, L.; Speck, J. S.; Pompe, W.; Foster, C. M.; Bai, G. R. *J. Appl. Phys.* **1998**, *83*, 2742–2753.
- (5) Zhang, J.-X.; Li, Y.-L.; Choudhury, S.; Chen, L. Q.; Chu, Y. H.; Zavaliche, F.; Cruz, M. P.; Ramesh, R.; Jia, Q. X. *J. Appl. Phys.* **2008**, *103*, 094111.
- (6) Ederer, C.; Spaldin, N. A. *Phys. Rev. B* **2005**, *71*, 060401(R).
- (7) Kubel, F.; Schmid, H. *Acta Crystallogr., Sect. B: Found. Crystallogr.* **1990**, *46*, 698.
- (8) Seidel, J.; Martin, L. W.; He, Q.; Zhan, Q.; Chu, Y. H.; Rother, A.; Gemming, S.; Lichte, H.; Yu, P.; Wang, F.; Catalan, G.; Scott, J. F.; Spaldin, N. A.; Ramesh, R. *Nat. Mater.* **2009**, *8*, 229.
- (9) Béa, H.; Bibes, M.; Ott, F.; Dupe, B.; Zhu, X.-H.; Petit, S.; Fusil, S.; Deranlot, C.; Bouzehouane, K.; Barthelemy, A. *Phys. Rev. Lett.* **2008**, *100*, 017204.
- (10) Martin, L. W.; Chu, Y.-H.; Holcomb, M. B.; Huijben, M.; Yu, P.; Han, S.-J.; Lee, D.; Wang, S. X.; Ramesh, R. *Nano Lett.* **2008**, *8*, 2050–2055.
- (11) Zaleski, A. V.; Frolov, A. A.; Khimich, T. A.; Bush, A. A. *Phys. Solid State* **2003**, *45*, 141–145.
- (12) Chu, Y.-H.; Zhan, Q.; Martin, L. W.; Cruz, M. P.; Yang, P. L.; Zavaliche, F.; Yang, S. Y.; Zhang, J.-X.; Chen, L. Q.; Schlom, D. G.; Lin, I. N.; Wu, T. B.; Ramesh, R. *Adv. Mater.* **2006**, *18*, 2307–2311.
- (13) Chu, Y.-H.; Cruz, M. P.; Yang, C.-H.; Martin, L. W.; Yang, P. L.; Zhang, J. X.; Lee, K.; Yu, P.; Chen, L. Q.; Ramesh, R. *Adv. Mater.* **2007**, *19*, 2662–2666.
- (14) Kalinin, S. V.; Shao, R.; Bonnell, D. A. *J. Am. Ceram. Soc.* **2005**, *88*, 1077–1098.
- (15) Xu, G.; Hiraka, H.; Shirane, G.; Li, J. F.; Wang, J.; Viehland, D. *Appl. Phys. Lett.* **2005**, *86*, 182905.
- (16) Xu, G.; Li, J.; Viehland, D. *Appl. Phys. Lett.* **2006**, *89*, 222901.
- (17) Grossmann, M.; Lohse, O.; Bolten, D.; Boettger, U.; Waser, R. *Mater. Res. Soc. Symp. Proc.* **2002**, *6880*, C3.4.1–C3.4.9.
- (18) Lebeugle, D.; Colson, D.; Forget, A.; Viret, M. *Appl. Phys. Lett.* **2007**, *91*, 022907.
- (19) Baettig, P.; Ederer, C.; Spaldin, N. A. *Phys. Rev. B* **2005**, *72*, 214105.
- (20) Chopdekar, R. V.; Takamura, Y.; Suzuki, Y. *J. Appl. Phys.* **2006**, *99*, 08F503.
- (21) Herranz, G.; Sánchez, F.; Garcia-Cuenca, M. V.; Varela, M.; Martinez, B.; Fontcuberta, J. *Mater. Res. Soc. Symp. Proc.* **2002**, *690*, F3.5.1F3.5.6.
- (22) Shepard, M.; McCall, S.; Crow, J. E. *J. Appl. Phys.* **1997**, *81*, 4978–4980.

NL900723J